Validation and Sensitivity analysis for a nasal spray deposition computational model

Hadrien Calmet[a], David Oks[a], Alfonso Santiago[a], Guillaume Houzeaux[a], Antoine Le Corfec[b], Laura Deruyver[b], Clement Rigaut[c], Pierre Lambert[c], Benoit Haut[c], Jonathan Goole[b]

[a]*Barcelona Supercomputing Centre,(BSC-CNS), Department of Computer Applications in Science and Engineering, Barcelona, Spain*

[b]*Department of Pharmaceutical Sciences, Université libre de Bruxelles, Brussels, Belgium*

[c]*Ecole polytechnique de Bruxelles, Université libre de Bruxelles, Brussels, Belgium*

Abstract

Validating numerical models against experimental models of nasal spray deposition is challenging since many aspects must be considered. That being said, it is a critical step in the product development process of nasal spray devices. This work presents the validation process of a nasal deposition model, which demonstrates a high degree of consistency of the numerical model with experimental data when the nasal cavity is segmented into two regions but not into three. Furthermore, by modelling the flow as stationary, the computational cost is drastically reduced while maintaining quality of particle deposition results. Thanks to this reduction, a sensitivity analysis of the numerical model could be performed, consisting of 96 simulations. The objective was to quantify the impact of four inputs: the spray half cone angle, mean spray exit velocity, breakup length from the nozzle exit and the diameter of the nozzle spray device, on the three quantities of interest: the percentage of the accumulated number of particles deposited on the anterior, middle and posterior sections of the nasal cavity. The results of the sensitivity analysis demonstrated that the deposition on anterior and middle sections are sensitive to injection angle and breakup length, and the deposition on posterior section is only, but highly, sensitive to the injection velocity.

Keywords: nasal spray, CFPD, experimental model, nasal drug delivery,

*Corresponding Author: hadrien.calmet@bsc.es

1. Introduction

Nasal drug delivery is an attractive approach to treat diseases such as sinusitis, allergic rhinitis, nasal polyposis or migraines [1, 2, 3]. In addition, the nasal cavity is a promising route for systemic drug delivery due to potential drug absorption through the porous endothelial membrane of the rich vascular capillary bed underneath the nasal mucosa [4, 5]. Nowadays, several investigations are in progress to create new intranasal vaccines to treat respiratory viruses such as SARS-CoV-2 [6, 7, 8].

Furthermore, the olfactory nerve, located on the top of the nasal cavity, represents a potential pathway to reach the central nervous system. Following this route, the drug reaching the olfactory area of the nose follows the path of the olfactory nerve to arrive to the brain. The main advantages of this pathway are the possibility to decrease the drug dose [9] and to treat neurologic diseases.

Numerical simulations (*in-silico*) using computational fluid dynamics (CFD) guided with experimental measurements (*in-vitro*) are an appealing approach that can reduce the cost and time related to device testing [10, 11]. CFD is an efficient tool to evaluate the performance of a nasal spray products on realistic nasal airway models under multiple conditions [12, 13, 14]. Recent investigations have characterized the performance of the nasal spray pump and assessed drug delivery to the nasal cavities [15, 16, 17, 18]. Kiaee et al. [19] found that particle diameter and particle injection speed were the most important parameters (other parameters were spray cone angle, particle injection location and spray release direction)

affecting deposition in seven adult nasal airways. In the present work four parameters are selected to evaluate the performance of the nasal spray device. The influence of the breathing conditions themselves during spray delivery on the uptake of the drugs has not been investigated as part of this study. Here the inhalation is a short burst of high flow rate (as a sniff) [12].

While most simulations are deterministic, engineering applications have many sources of uncertainty arising from multiple factors such as subject variability, initial conditions or system surroundings. Furthermore, the numerical model itself can introduce large uncertainties due to the assumptions and the numerical approximations employed [20]. Without the ability to accurately estimate uncertainties in a study, decision makers will be ill advised. Recently published standards as the American Society of Mechanical Engineers (ASME) VV 40 standards [21, 22] address this fundamental disconnect between simulations and practical applications by defining a theoretical framework to assess the numerical and experimental uncertainty. This provides a powerful predictive tool for decision makers. While stringent processes call Verification, Validation and Uncertainty Quantification (VVUQ) requires a number of intricate and correlated steps, the first tool to understand the problem is executing a Sensitivity Analysis (SA). The SA provides a deep understanding of the model behaviour showing the statistical correlation between the model inputs and the Quantities of Interest (QoI, also called outputs). Despite the amount of data obtained from a thorough SA, it is an undeniably computationally expensive process, as hundreds or thousands of simulation executions are required. This is why, a supercomputing infrastructure, such as Marenostrum 4, and a highly efficient high performing computer (HPC) code are necessary for this step.

The objective of this study is to validate the numerical model against the experimental model of nasal spray deposition with good agreement. Based on this, the study aims to create a reduced order model, lowering the computational cost while maintaining the quality of particle deposition results. Finally, an analysis is carried out on the sensitivity of the nasal spray device numerical model to variations in input parameters.

2. Materials and Methods

2.1. Nasal cast and spray device

The human nasal cavity was reconstructed from computed tomography (CT) scans collected from Erasme Hospital in Brussels. The report of the consultant radiologist declared that the nasal cavity was clear and of normal appearance. The protocol of the study has been approved by the hospital's ethical committee (Protocol P2022/075, agreement valid from 19/04/2022 til 31/12/2027). To process CT-scan images, different programs were used: (i) Python scripts that clean scans and converts images into monochromatic scale, (ii) ImageJ® to remove the sinuses to keep only the nasal cavity, (iii) InVesalius® to generate an STL file of the cavity, (iv) MeshLab® to repair and edit meshes to optimally prepare the model for 3D printing, and (v) FreeCAD® to build the different parts to be printed from the previously encoded 3D geometry.

The nasal cavity geometry reconstructed from CT scans was used to 3D-print a nasal cast used in the experimental studies presented below. The nasal cast (see Fig 1) is composed of five pieces, corresponding to (A) the nostrils, (B) the olfactory zone, named upper part, (C) the middle turbinates, called middle part, (D)

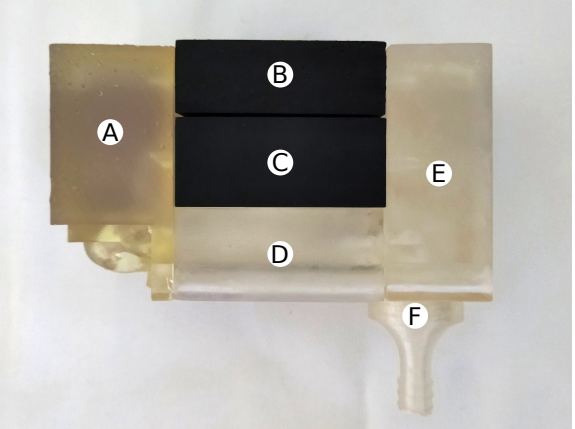

Figure 1: 3D-printed nasal model.(A) the nostrils, (B) the olfactory zone, (C) the middle turbinates, (D) the lower turbinates and (E) the nasopharyngeal zone, and (F) the pump adaptor containing a filter. Parts (B) and (C) contains the soft nasal valve. The nostrils are also printed in flexible resin.

the lower turbinates, called lower part, and (E) the nasopharyngeal zone called pharynx in this study. These sections were assembled to form the full *in vitro* model, see Fig 2b,c. For the 3D printing, the Form 3D SLA printer (Formlabs®, Somerville, MA, USA) was used with Formlabs Clear® resin to produce the different parts of the nasal cast. For further information regarding the nasal cast construction, refer to [23].

To better mimic the adhesion of the powder on the mucosa, the nasal cast was coated with a solution of Poloxamer® 407 (25 % w/w) in simulated nasal electrolyte solution (SNES)[23]. This mucus is liquid under 18 °C and in a gel form above this temperature. A comparison of the artificial mucus properties with human nasal physiological mucus is provided in table 1.

For several reasons Caffeine was used to study the powder deposition in the nasal cast. Caffeine has a good solubility in water (2.17 g/100 mL at 25°C) and ethanol (1.51 g/100 mL) [27], which makes it easy to handle. The solubility in ethanol is important to allow the recovering and the solving of the drug and thus vi-

	Artificial mucus	Physiological mucus	Reference
pH	6.406 ± 0.004	$5.5 - 6.5$	England, 1999 [24]
Osmolarity	317.7 ± 0.3 mOsm/kg	216 mOsm/kg	Joris, 1993 [25]
Viscosity	77 ± 5 Pa · s	12 Pa · s	Puchelle, 1983[26]

Table 1: Comparison of the physico-chemical properties between artificial mucus used in this study and physiological mucus.

sualizing its deposition profile in the different pieces of the nasal cast via spectrophotometry. The ethanol was preferred to water, despite the lower solubility of caffeine because of its ability to dissolve the artificial mucus used to coat the cast. In addition, caffeine is easily quantifiable by UV spectroscopy at a wavelength of 274 nm. The device used to inject 20 mg of pure caffeine powder into the nasal cast is a single-dose unidirectional device supplied by Aptar® UDS (Aptar Pharma, Le Vaudreuil, France), see Fig 2a. For the experiments, the caffeine was sifted through a 123 µm sieve to produce particles with adequate size.

To fix the spray in a precise position, supports were designed and printed as shown in Fig 2b,c. The support, which uses the principles of [23], is used so that the spray directly targets the olfactory zone to produce greater deposition there. On the right side, the sagittal angle of the spray was 39° from the vertical and the coronal angle was 21°, aiming to the septum. On the left side, the sagittal angle of the spray was 29° from the vertical and the coronal angle was 5°, aiming to the septum. In both nostrils, the spray is inserted as deeply as possible while keeping the desired angle of the spray tip.

The aerodynamic diameter, as well as the dispersion of the plume, were evaluated using a Spraytec® laser diffraction system (Malvern Instrument, Marvern, Worcestershire, UK) in combination with the RTSIzer software. At the time of taking measurements, the spray was held vertically by a support at a distance of

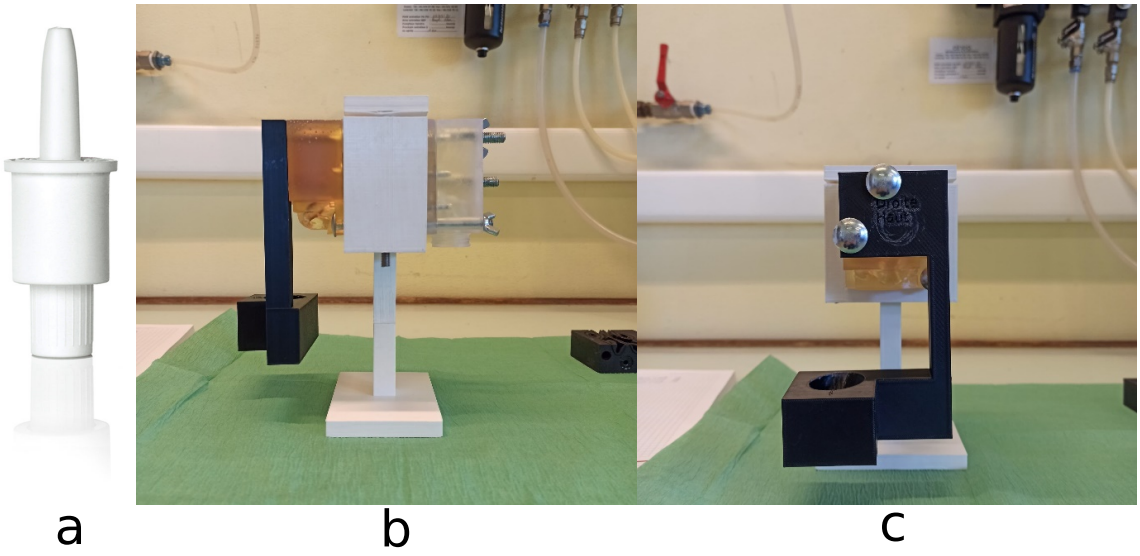

Figure 2: a) Single-dose unidirectional device by Aptar b) Side view and c) Front view of the spray support.

7 centimeters from the laser source using a test duration of 300 ms and an acquisition rate of 2500 Hz. Each measurement was repeated in triplicate. The results obtained for Dv10, Dv50, Dv90 and Span are presented in Table 2. In addition to plume measurement of the caffeine spray at the exit of the device, velocity and plume angle were also measured via high-speed imaging. By way of a brief overview, the plume was captured by an IDT motion pro Y3 camera (Integrated Design Tools, Pasadena, CA, USA), equipped with a Nikon AF micro-Nikkor 60 mm f/2.8 D lens (Nikon, Tokyo, Japan). The plume angle was then measured using a Sobel algorithm and Hough filter for edges detection and the speed was measured by the displacement of the front of the plume between two consecutive frames.

	Mean ± standard deviation
Dv10 (µm)	10.4 ± 0.5
Dv50 (µm)	25 ± 1
Dv90 (µm)	54 ± 3
Span	1.76 ± 0.03
Velocity ($m\,s^{-1}$)	49 ± 6
Angle (°)	17 ± 2

Table 2: Parameters of the spray: Distribution of particle size, velocity and angle. The results are expressed by mean and standard deviation and were achieved in *triplicate*.

2.2. Experimental measurements of nasal deposition

Airflow was induced with air pumps within the nasal cast to mimic breathing. To model a rapid and short inhalation also called a sniff, a flow rate of $60\,L\,min^{-1}$ was used [28, 29] for a duration of 1.2 s. To do so, the whole cast was connected via the nasopharynx exit to a TPK 2000 flow controller, itself connected to two HCP5 pumps (Copley Scientific, Nottingham, UK).

Three tests were performed following the same protocol:

1. Each of the five pieces were coated, previously placed in the refrigerator for ten minutes, with a layer of artificial mucus through a micro-pipette. The liquid was poured until a capillary film formed on the whole surface. Then, the excess mucus was allowed to drip out of the cast.
2. Once the artificial mucus deposited, the pieces were thermalised to room temperature.
3. The 3D model was assembled while placing the spray holder with the delivery device. The assembly was then placed in a support that allowed the model to be kept horizontal. Then the cap was attached, equipped with a filter to recover particles that would leave to the lower respiratory tract.

4. The entire device was then connected to the flow controller and pumped. The flow rate was set up at $60\,\mathrm{L\,min^{-1}}$ for 1.2 s.
5. The spray was unloaded manually when the flow was well established. After the instillation, the pumps were cut.
6. The 3D model was disassembled and each slice was placed in a beaker which was then placed in the fridge for ten minutes to liquefy the gel.
7. The slices were rinsed with ethanol to dissolve the gel and the caffeine. The volumes of ethanol used were 20 mL for the nostrils, 20 mL for the olfactory region, 50 mL for the middle turbinates, 25 mL for the lower turbinates, 10 mL for the nasopharynx, and 10 mL for the post-nasal filter.
8. All the beakers were put in the ultrasonic bath.
9. The samples were quantified by spectrophotometry.

Table 3 shows the results as a percentage of deposition relative to the total mass of powder instilled and deposited in each piece of the nasal cast, see Fig. 1.

	Mean ± standard deviation
Output	3.7±0.5%
Pharynx	6.5±0.5%
Upper part	7±3%
Middle part	74±4%
Lower part	5.4±0.5%
Nostril	3±1%

Table 3: Ratio of the amount of caffeine deposited in the different pieces of the nasal cast to the total amount instilled (expressed as a percentage). The results are expressed as an average ± standard deviation and were performed in *triplicate*.

2.3. *Numerical simulations*

The experimental setup was numerically modelled using computational fluid dynamics to solve the flow and particle transport models to obtain the caffeine deposition. The computational domain was set up as a semi-hemisphere surrounding the bottom part of the patient's face with a radius of 0.2 m to ensure a correct inflow in the vicinity of the nostrils. A no-slip boundary condition was imposed on all airway walls and the flat surface of the semi-hemisphere to mimic the effects of the bottom part of the face and the experimental setup. The inhalation time-profile used is the saw tooth pattern, with a peak volumetric flowrate of 60 L min^{-1} see (Fig 4b) to reproduce the magnitude of a rapid and short inhalation, also called a sniff [29, 28]. The transient inflow was prescribed as a time varying uniform velocity with a direction normal to the semi-hemisphere, and imposed as a Dirichlet boundary condition. A zero-traction outflow boundary condition was imposed at the outlet of the naso-pharynx (the surface is free from external stress). Given the complexity of the geometry, an unstructured mesh was constructed using the ANSYS ICEM CFD meshing software (ANSYS Inc., USA). The mesh used in this study is hybrid, made of tetrahedrons to fill the core of the nasal cavity and layers of prisms to resolve the near-wall high velocity gradients, see Fig.3. Aspects of the mesh generation procedure are discussed in further detail in the appendix section.

The computational mechanics code Alya [30], developed at Barcelona Supercomputing Center, was used to simulate the Navier-Stokes equations. Different numerical models were employed in this study: a large eddy simulation (LES), an implicit large eddy simulation (iLES), and the "freeze" model, which corresponds to transporting the particles with a constant velocity field. This later is obtained

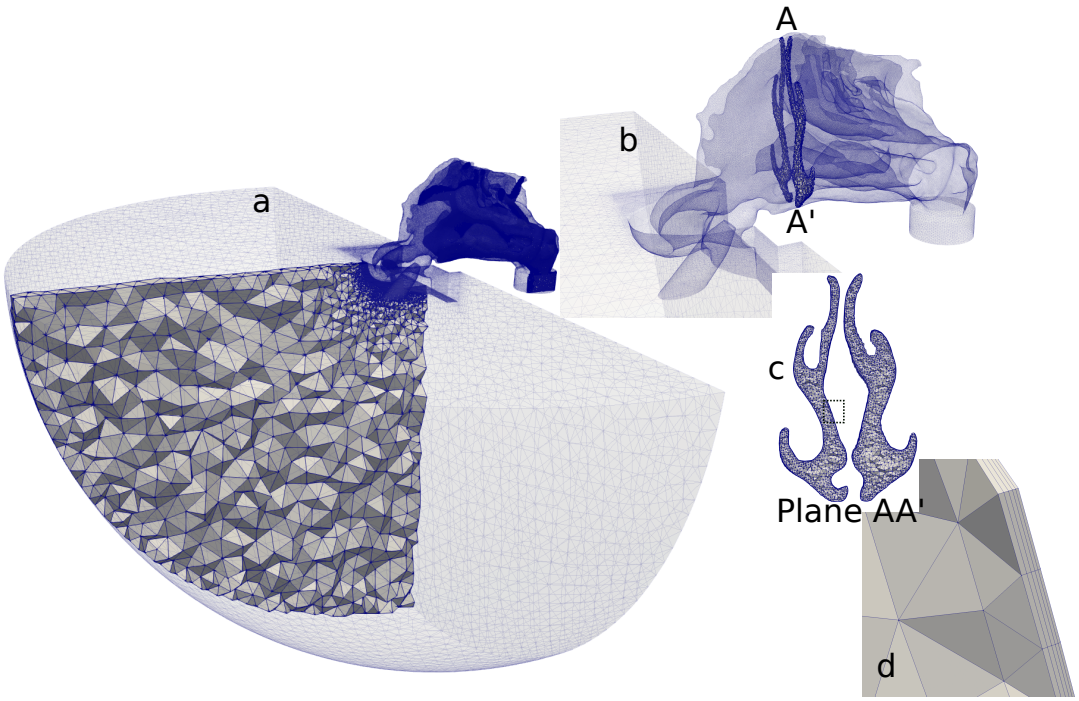

Figure 3: Grid generation topology for the mesh M2 used in this study: a) general view of the 3D computational domain, b) closer view of the nasal cavity, the spray nozzle and the location of the plane AA', c) coronal view of plane AA' and d) wall clustering feature of the selected slice.

Case	Mesh	Model	Time step strategy	N_{CPU}	Δt(s)
C1	M1	LES	Explicit(RK4)	240	$1.3e^{-6}$
C2	M1	implicit LES	Implicit(BDF2)	240	$1.0e^{-4}$
C3	M1	none	Newton-Raphson	240	$1.0e^{-4}$

Table 4: Summary of numerical model parameters, from left to right: case name, mesh employed, turbulence model, time stepping strategy, number of CPUs employed, time step size.

by averaging the velocity field starting 5 ms before and ending 5 ms after the peak flowrate ($60\,\mathrm{L\,min^{-1}}$) of the sawtooth, see Fig 4b. The "freeze" field is obtained from LES simulation, only the particle transport is solved, resulting in a significantly lower computational cost per simulation.

For the LES simulation, the wall-adapting local-eddy viscosity model (WALE)[31] was applied. This model provided good results in previous simulations of respiratory airways and provides faster results compared to more computational demanding models like the dynamic Smagorinsky, see [32]. Details of the model and parameters used in the simulations are given in Table 4. Further details of the numerical methods for the LES can be found in the Appendix section or [33]. We have adopted the term iLES in this study for the modelling approach where turbulence effects are neglected (since it is widely used in the respiratory flow community [34, 35, 36]). In the Alya code, when no explicit turbulence model is used, the model introduces numerical dissipation leading to what is known as an implicit LES model (iLES) [37]. Moreover, for the simulations with larger time steps than that required for a well resolved LES simulation, the method can be classified as a Very Large Eddy Simulation (VLES). A stabilized finite element method, based on the Variational MultiScale (VMS) method [38] was used for iLES model.

Particle transport and deposition modelling

Particle transport was simulated in a Lagrangian frame of reference, following each individual particle. The main assumptions of the model are:

- particles are sufficiently small and the suspension is sufficiently dilute to neglect their effect on airflow, *i.e*: one-way coupling,
- particles are spherical and do not interact with each other,
- particle rotation is negligible,
- thermophoretic forces are negligible, and
- the forces considered are drag $\boldsymbol{F}_d$, gravitational and buoyancy $\boldsymbol{F}_g$ forces.

The transport of particles was solved by solving Newton's second law, and by applying a series of forces

$$\boldsymbol{a}_p = (\boldsymbol{F}_d + \boldsymbol{F}_g)/m_p. \tag{1}$$

where $\boldsymbol{a}_p$ and $m_p = \rho_p V_p$ are the particle acceleration and mass. Here ρ_p is the particle density and $V_p = \frac{\pi}{6} d_p^3$ its volume and d_p its diameter. The particle position and velocity will be indicated as $\boldsymbol{x}_p$ and $\boldsymbol{u}_p$ respectively. The equation for the drag force assumes the particle has reached its terminal velocity, and is given by

$$\boldsymbol{F}_d = -\frac{\pi}{8} \mu d_p C_d \mathrm{Re}(\boldsymbol{u}_p - \boldsymbol{u}_f), \tag{2}$$

where μ is the dynamic viscosity, related to the kinematic viscosity $\nu = \mu/\rho$, with ρ the fluid density. The particle Reynolds number, indicated by Re, involves its

relative velocity with respect to the fluid:

$$\mathrm{Re} = \frac{|\boldsymbol{u}_p - \boldsymbol{u}_f| d_p}{\nu}.$$

The drag coefficient uses Ganser's formula [39]:

$$\begin{aligned}
C_d &= \frac{24}{\mathrm{Re}\, k_1}(1 + 0.1118(\mathrm{Re}\, k_1 k_2)^{0.6567}) + 0.4305 \frac{k_2}{1 + 3305/(\mathrm{Re}\, k_1 k_2)}, \\
k_1 &= \frac{3}{1 + 2\psi^{-0.5}}, \\
k_2 &= 10^{1.84148(-\log_{10}(\psi))^{0.5743}}, and \\
\psi &= \text{sphericity (= 1 for a sphere).}
\end{aligned}$$

The gravity and buoyancy forces contribute to the dynamics of the particle when there is a density difference:

$$\boldsymbol{F}_g = V_p \boldsymbol{g}(\rho_p - \rho),$$

with $\boldsymbol{g}$ being the gravity vector. Further details about particle transport and deposition modeling are available in [40, 41]. Once the particle has crossed an outlet boundary element, the particle is out of the computational domain and removed from the simulation. Furthermore, particles are deposited as soon as they get in contact with wall boundaries. The validation of the particle deposition aspect is provided in the Appendix section.

Nasal spray model

The assumed sprayed particle conditions in this study were: a spray half cone angle of 17°, a mean spray exit velocity of $49.0\,\mathrm{m\,s^{-1}}$ and a solid-cone type injection. The particle sizes were determined with a log-normal distribution, defined by the probability density function

$$f(x) = \frac{1}{\sqrt{2\pi}x \ln \sigma_g} \exp\left[-\frac{(\ln x - \ln x_{50})^2}{2(\ln \sigma_g)^2} \right] \tag{3}$$

where x is the particle diameter. The log normal distribution median was initially set to x_{50}, also known as $Dv50$ which is the volume median diameter, and $\ln \sigma_g$ is the standard deviation, where $\sigma_g = 1.76\,\mu\mathrm{m}$. The resulting particle size distributions for $Dv50 = 25.5\,\mu\mathrm{m}$ are shown in Fig4a. The total number of particles released in one actuation is approximately 0.4 million.

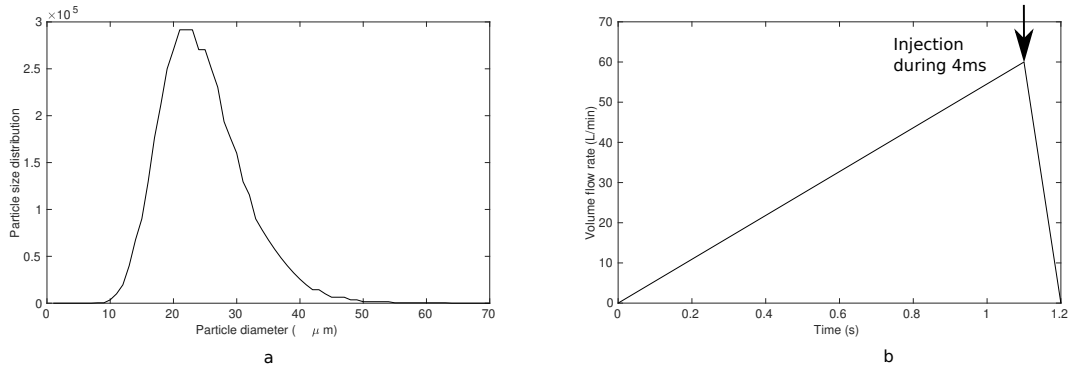

Figure 4: a) Log-normal distribution function showing the profile for median of $Dv50 = 25.5\,\mu\mathrm{m}$, b) Volume flow rate of the pump used to mimic the human sniff airflow.

A commercial model of the nasal spray Aptar was included, basing its location and geometry on the STL file and experimental device. The nozzle length was set to 2 cm.

Particles were introduced into the computational domain from a breakup length of 5 mm from the nozzle exit (as the atomization stage is not considered) [42] at the start of the simulation and re-injected every 0.1 ms until the last injection time (4 ms) thus a total of 40 injections (see Fig 4b). This resulted in a total of 0.4 million particles released during the entire simulation.

2.4. Sensitivity analysis

A sensitivity analysis was carried out to quantify the sensitivity of the numerical model to variations in inputs. To do so, four model input parameters and three output quantities of interest were considered. The four model inputs are the spray half cone angle, mean spray exit velocity, breakup length from the nozzle exit and the diameter of the nozzle spray device. The three outputs are the percentage of the accumulated number of particles deposited on the anterior, middle and posterior sections of the nasal cast at the end of the simulation.

The Dakota software (Sandia National Laboratories) [43] was used to set up and execute the sensitivity analysis. DARE, a tool developed at BSC that acts as an automation software with the tasks of encoding, decoding, submitting the jobs to the cluster and retrieving the results, was used to connect Dakota with Alya [44]. To efficiently sample the parameter space and avoid aliasing distortions, a Latin hypercube sampling (LHS) method was employed, with a sample size of 96 cases. LHS is a statistical method for generating a near-random sample of parameter values from a multidimensional distribution, which ensures that the set of random numbers generated is a good representation of the real variability of parameters.

	LES	iLES	freeze
Middle part	26.1	25.9	26.1
Lower part	70.3	70.5	70.4
Nostril	3.5	3.4	3.4
Upper part	4.5E-03	9.5E-03	1.0E-02
Pharynx	4.8E-02	4.7E-02	5.3E-02
Output	4.7E-03	6.2E-03	2.3E-04
CPU/ite(s)	0.5	3	0.1
N_{ite}	227750	3000	1000
time (h)	33	8	0.05

Table 5: Particle depositions expressed as percentage for each nasal cast part and each numerical method. At the bottom: CPU/ite: execution time per iteration, N_{ite}: number of iterations, and time: total execution time (0.3 s).

3. Results

3.1. Computational cost reduction

In order to feasibly run 96 cases for the sensitivity analysis, it is paramount to reduce the computational cost of numerical simulations while maintaining acceptable fidelity in particle depositions. The different numerical methods employed have been explained above, and further detailed information is available in the Appendix section. Details of the model and parameters used in the simulations are given in Table 4. The results of particle depositions are compared based on the separated pieces of the nasal cast including nostril, lower part, middle part, upper part, pharynx, and the particles going out of the domain which are called output in Table 5.

The total physical time simulated was 0.3 s, starting the simulation at 0.9 s of the saw tooth profile and ending at 1.2 s (Fig 4b), where the order of velocity magnitude in the nose is approximately $10\,\mathrm{m\,s^{-1}}$. We assume that 0.2 s before the

injection was enough to establish the transient flow from the pump. As it can be observed in Table 5, the difference between the different numerical methods is minimum. If the LES simulation is taken as a reference, the difference observed with both other methods is less than 0.3%. Regarding the computational cost, a significant cost reduction is obtained from the LES to the iLES method (approximately 4x). Moreover, a drastic 600x reduction is observed for the freeze method, with a relative error difference of less than 0.2%. Note that a deeper comparative analysis has been carried out by the same authors between LES and iLES on fluid variables such as pressure and velocity, and including a turbulence analysis along the respiratory cycle, without particle transport and deposition [45].

The deposition of polydisperse particles with $Dv50 = 25.5\,\mu m$ injected at $49\,m\,s^{-1}$ appears not to be sensitive to the use of the different numerical methods. These are large droplets with high velocity, which leads to high momentum transport. As a consequence, their trajectory is not strongly affected by subscale dynamics. For this same reason, most of these particles are deposited by inertial impaction. Differences could be observed for the smallest particles, that is particles with low inertia. However, since few particles of this size are injected, they do not produce significant changes in global particle deposition patterns. Since the choice of the numerical method does not significantly affect the output quantities of interest, and since the freeze method is 600x less costly than LES, the freeze method was chosen to carry out the large number of simulations executed for the present sensitivity analysis.

3.2. Validation

Validating experimental and numerical results is a challenging task in the sense that multiple sources of error originate on either side. Uncertainties may be epistemic or aleatory. Epistemic uncertainties arise from lack of knowledge of the system or problem of interest, while aleatory uncertainty refers to uncertainty caused by probabilistic variations in a random event [46]. In numerical simulations epistemic uncertainties may arise as input, model or numerical uncertainties [47]. Input uncertainties arise from some parameters not being well defined, such as particle dimensions, number of particles injected, flowrate at inlet, etc. Model uncertainties result from alternative mathematical models, numerical methods, formulations, structure, or implementations. For instance, the Navier-Stokes equations implemented in two codes may yield different results when modeling the same problem. Numerical uncertainties result from the influence of discretization and iterative convergence errors, such as mesh resolution and time step size. This is the only type of uncertainty that cannot be eliminated, but only minimized or bounded in a simulation. In experimental studies, epistemic uncertainties also must be considered. Some of these are data pre-processing uncertainties when selecting and cleaning inputs/outputs, parameter uncertainties which appear when the model parameter values are specified under imprecise knowledge or lack of direct measures, structural uncertainties such as the differences between a nasal cast and the actual human nasal airways. In experiments, aleatory uncertainties include measurement uncertainty due to lack of resolution in instruments or human error, and sampling uncertainty due to under-sampling a large population of interest.

Literature on the validation of particle deposition in the human nasal cavity is

scarce [18, 48]. In contrast, extensive literature exists on particle deposition in the throat [49, 10, 11]. The experimental setup allows measuring the deposition on each independent region thanks to the separate nasal cast pieces, see Fig 1. Most

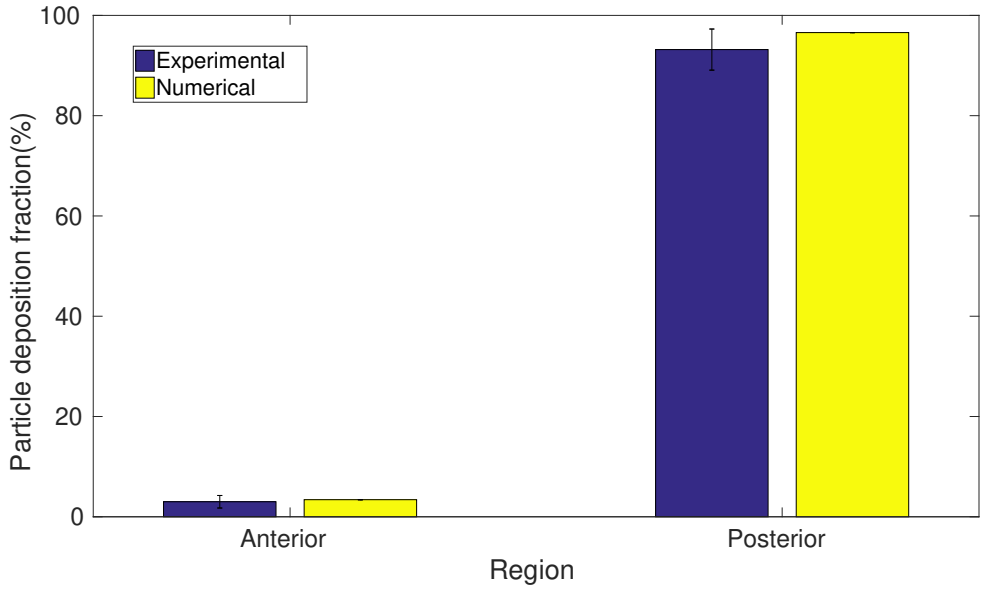

Figure 5: Comparison of the numerical regional particle deposition fraction with the experimental measurements.

of the time the authors prefer to segment the airways into two regions [18, 50] to obtain an anterior and posterior part. In this study, we segment in two regions, and then in three. When using three regions, significant differences are observed in the particle deposition regional fractions, especially in the posterior region. Fig 5 shows the comparison using two regional particle deposition fractions with experimental measurements. Anterior region is the nostril part (A); Posterior region encompasses upper (B), middle (C), lower (D) and naso-pharynx (E) parts, see Fig 1. Good agreement is observed between the *in-silico* and *in-vitro* results for both regions, see Table 6.

	Anterior (%)	Posterior(%)
Experimental	3.1±1	93.1±4
Numerical	3.4	96.5
Relative error	10.0	3.6

Table 6: Particle deposition fractions in anterior and posterior sections for the experimental and numerical studies, and the relative error among them.

Taking advantage of the different nasal cast pieces, airways can be further split into three regions of interest, namely anterior, middle and posterior, with this time middle region encompassing upper (B), middle (C) and lower (D) parts see Fig 1. Discrepancies are now clearly observed in the middle and posterior regions. These differences could be produced by different sources of uncertainties, such as definition of boundary conditions. In particular, one difference could be explained by the two-way coupling missing in the numerical model, that is the mutual exchange of forces between fluid and particles. In [18] authors explained that the two-way coupling significantly increased the travel distance of smaller particles from sprayed particles and thus increased the particle deposition fraction in the posterior part of the airways. The implementation of the two-way coupling will be the scope of a future study. Furthermore, a significant difference exists in the surface of the airways: To capture the caffeine deposited on the surface, a coating gel is used on the nasal replica which in the numerical model is treated as a wet and rigid wall. Note that experimental results [50] showed that a wide range of variability exists for drug delivery depositions in the posterior region. If this variability is dominantly a consequence of the variability among patient-specific geometries, then using the same patient-specific geometry in *in-silico* and *in-vitro* studies should account for differences. In any case, this observation manifests how challenging it is to reproduce physiological depositions

	Anterior (%)	Middle (%)	Posterior(%)
Experimental	3.1±1	86.7±4	6.5±1
Numerical	3.4	96.5	0.01
Relative error	10.0	11.3	99.8

Table 7: Particle deposition fractions in anterior, middle and posterior sections for the experimental and numerical studies, and the relative error among them.

in either *in-silico* or *in-vitro* studies.

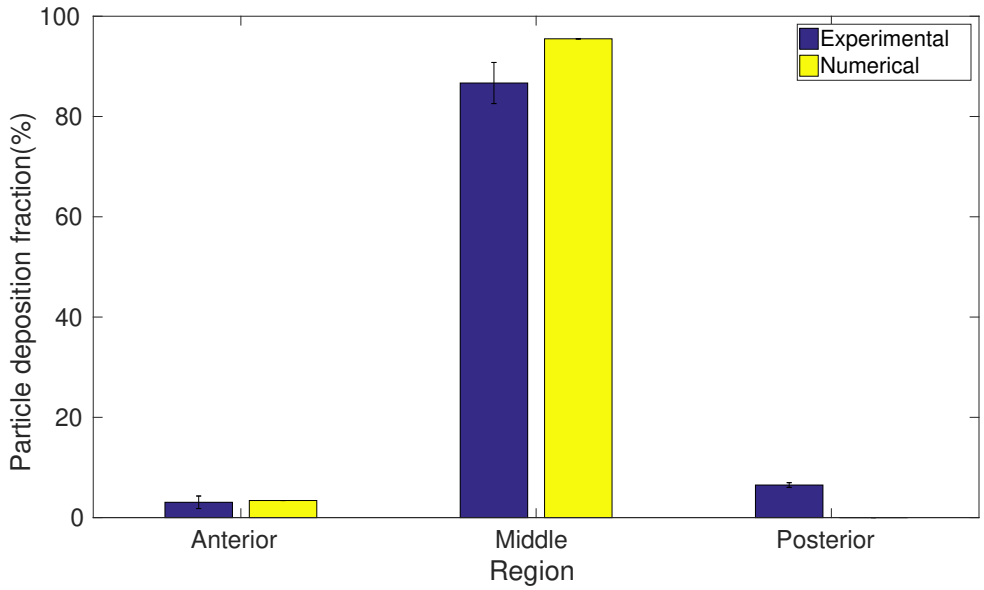

Figure 6: Comparison of the numerical regional particle deposition fraction with the experimental measurements.

To have a different perspective on this issue and as a third objective of this work, we propose a sensitivity analysis on four key parameters of the nasal sprayed particles: the spray half cone angle, the mean spray exit velocity, the breakup length from the nozzle exit and the diameter of the nozzle spray device.

3.3. *Sensitivity analysis*

In the numerical approach, all the parameters from a nasal spray device can be modified rapidly and with low effort compared to the experimental approach. Here four inputs are selected, mainly to focus the sensitivity analysis on the discrepancies observed in the posterior deposition results. The three outputs are the percentage of the accumulated number of particles deposited on the anterior, middle and posterior sections of the nasal cast. Thanks to the computational cost reduction, the entire sensitivity analysis took only 6 hours to execute 96 simulations. Fig 7 shows a local sensitivity analysis via Pearson coefficients which

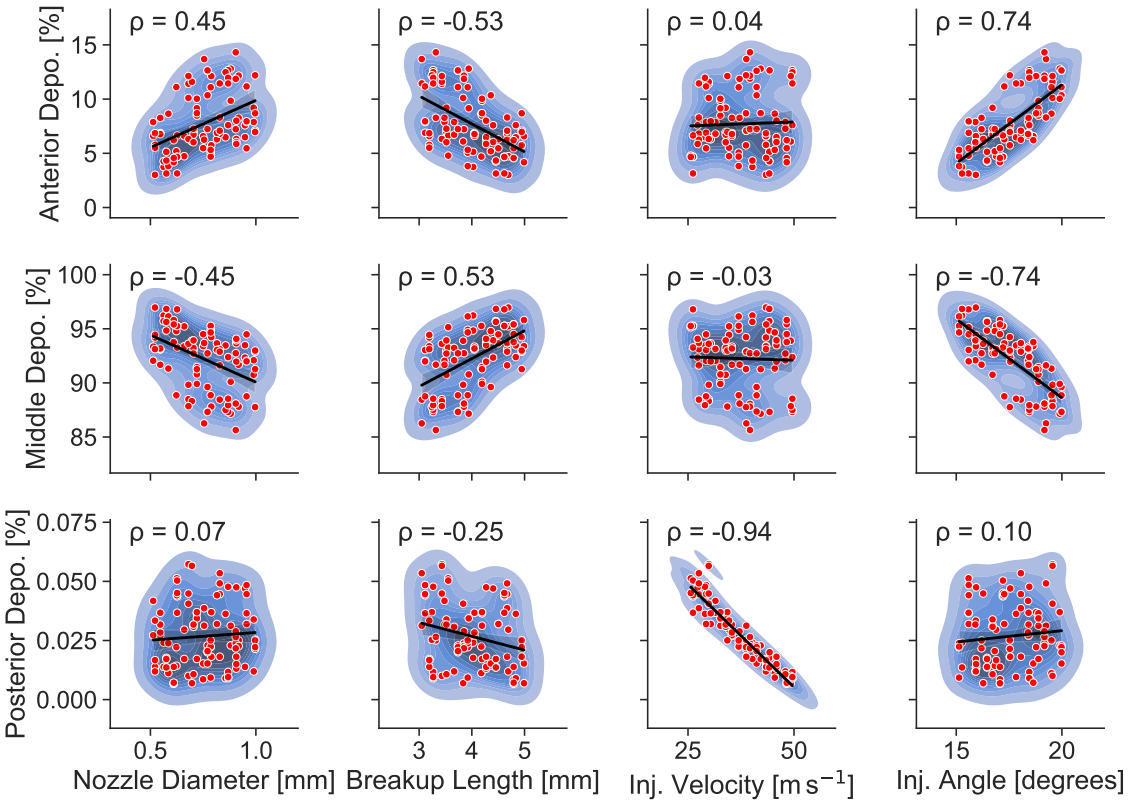

Figure 7: Scatter plots, with Pearson's linear correlation coefficient ρ shown in the top left corners.

Inputs	Nozzle Diameter(mm)	Breakup Length(mm)	Injection velocity(m/s)	Injection angle(°)
Lower bound	0.5	3	25	15
Upper bound	1.0	5	50	20

Table 8: Table of model inputs.

measure the strength of a linear association between an input and an output. The linear correlation coefficient ρ is shown in the top left corner of each plot. This number which ranges between -1 to 1 expresses the degree of correlation between two variables. A value of $\rho = 1$ implies a high correlation, 0 no correlation and -1 a high inverse correlation. The variations of the inputs are shown in Table 8 where the ranges are chosen to cover large variations that can be observed in commercial nasal spray devices. Breakup length is the distance where the particles are introduced into the computational domain from the nozzle exit as the atomization stage is not considered. Note that injection velocity of commercial products is rarely as high, as $50\,\mathrm{m\,s^{-1}}$. At the first glance of Fig 7, we observe a high correlation between the injection angle and the anterior deposition, an expected result, and a high inverse correlation with the middle deposition. The most important inverse correlation observed is between the posterior deposition and the injection velocity. More deposition in the posterior part is produced by less velocity which is an interesting result even if the percentage of deposition is very low. It seems to indicate that the particles mustb be slowly injected in order for them to have a chance to reach the posterior part. Otherwise, they are deposited before. On the other hand, injection velocity is not correlated with the deposition on the anterior and middle parts since the lower value ($25\,\mathrm{m\,s^{-1}}$) is high enough for pure impaction on these regions.

To quantify the effect of uncertainty in the knowledge of inputs on the outputs

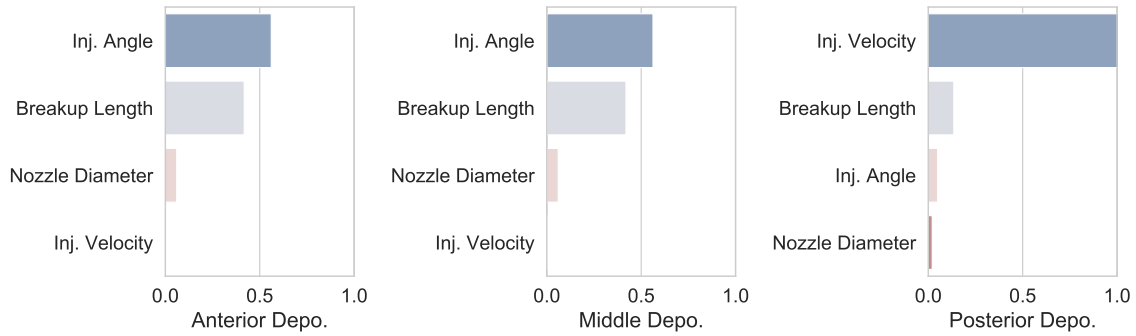

Figure 8: Total Sobol indices tornado plots for the 4 input variables and the 3 outputs.

of a model, it is useful to consider the Sobol indices [51]. These indices provide information on how the variance of model output is affected by variances of each input. It is a global form of sensitivity analysis that handily takes into account complex factors like nonlinearities, input interactions, and sample dispersion. In particular, the total Sobol index $ST_i(Y)$ quantifies the effect of the variance of an input variable X_i and its interactions with other inputs X_j $(j \neq i)$, on the variance of an output variable Y. A further description of this index is given in the Appendix. The total Sobol indices for each output as a function of inputs are shown in Fig 8 in the form of tornado plots. The larger the value of the index, the more the variation of that input affects the variation of the output. The anterior and middle depositions are sensitive at injection angle and breakup length which is coherent with the results obtained by the Pearson's correlation analysis. Moreover, the posterior deposition is only, and highly, sensitive to the injection velocity.

The results presented demonstrate the high potential of the employed sensitivity analysis tools to condense large amounts of data to the most relevant information subsets. It may seem redundant to run both Pearson's SA and the global SA, but they provide different points of view of the same problem, since the former quan-

tifies correlations between expected values of inputs on outputs, while the latter quantifies the effect of variances of inputs on output. Furthermore, the calculation of total Sobol indices requires the evaluation of high-order integrals. These complex numerical methods are within the reach of all readers. Therefore, the Pearson linear correlation analysis provides a tool allowing easy access comparison for future related works.

4. Conclusion

Up to 96 runs were carried out to evaluate the effect of four key parameters of the nasal sprayed particles by quantifying the impacts on the particles deposited on the anterior, middle and posterior sections of the nasal cavity. Results presented showed that the anterior and middle depositions sections are sensitive to injection angle and breakup length and that the posterior deposition section is only, and highly, sensitive to the injection velocity. Despite the limited inputs of this sensitivity analysis, this study demonstrates the potential of this tool to gain accuracy in testing nasal drug delivery products.

References

[1] P. G. Djupesland, Nasal drug delivery devices: characteristics and performance in a clinical perspective—a review, Drug delivery and translational research 3 (2013) 42–62.

[2] M. S. Dykewicz, D. L. Hamilos, Rhinitis and sinusitis, Journal of Allergy and Clinical Immunology 125 (2010) S103–S115.

[3] S. Le Guellec, S. Ehrmann, L. Vecellio, In vitro–in vivo correlation of in-

tranasal drug deposition, Advanced Drug Delivery Reviews 170 (2021) 340–352.

[4] A. Hussain, Mechanism of nasal absorption of drugs., Progress in clinical and biological research 292 (1989) 261–272.

[5] L. Illum, Nasal drug delivery: new developments and strategies, Drug discovery today 7 (2002) 1184–1189.

[6] J. V. Wilkins, L. Golshahi, N. Rahman, L. Li, Evaluation of intranasal vaccine delivery using anatomical replicas of infant nasal airways, Pharmaceutical research 38 (2021) 141–153.

[7] H. Zhang, Z. Yang, J. Xiang, Z. Cui, J. Liu, C. Liu, Intranasal administration of sars-cov-2 neutralizing human antibody prevents infection in mice, bioRxiv (2020).

[8] J. Xi, Development and challenges of nasal spray vaccines for short-term covid-19 protection, Current pharmaceutical biotechnology (2022).

[9] B. Forbes, R. Bommer, J. Goole, M. Hellfritzsch, W. De Kruijf, P. Lambert, G. Caivano, A. Regard, F. Schiaretti, M. Trenkel, et al., A consensus research agenda for optimising nasal drug delivery, Expert opinion on drug delivery 17 (2020) 127–132.

[10] Y. Feng, H. Hayati, A. J. Bates, K. Walter, L. Matthias, B. Odo, O. Ramiro, K. Gerda, Clinical cfd applications 2, in: Clinical and Biomedical Engineering in the Human Nose, Springer, 2021, pp. 225–253.

[11] P. Koullapis, F. Stylianou, C.-L. Lin, S. Kassinos, J. Sznitman, In silico methods to model dose deposition, in: Inhaled Medicines, Elsevier, 2021, pp. 167–195.

[12] H. Calmet, K. Inthavong, B. Eguzkitza, O. Lehmkuhl, G. Houzeaux, M. Vázquez, Nasal sprayed particle deposition in a human nasal cavity un-

der different inhalation conditions, PloS one 14 (2019) e0221330.

[13] C. Kleinstreuer, Z. Zhang, J. Donohue, Targeted drug-aerosol delivery in the human respiratory system, Annu. Rev. Biomed. Eng. 10 (2008) 195–220.

[14] P. W. Longest, K. Bass, R. Dutta, V. Rani, M. L. Thomas, A. El-Achwah, M. Hindle, Use of computational fluid dynamics deposition modeling in respiratory drug delivery, Expert opinion on drug delivery 16 (2019) 7–26.

[15] S. Basu, L. T. Holbrook, K. Kudlaty, O. Fasanmade, J. Wu, A. Burke, B. W. Langworthy, Z. Farzal, M. Mamdani, W. D. Bennett, et al., Numerical evaluation of spray position for improved nasal drug delivery, Scientific reports 10 (2020) 1–18.

[16] S. Chari, K. Sridhar, R. Walenga, C. Kleinstreuer, Computational analysis of a 3d mucociliary clearance model predicting nasal drug uptake, Journal of Aerosol Science 155 (2021) 105757.

[17] K. Inthavong, J. Tu, C. Heschl, Micron particle deposition in the nasal cavity using the v2–f model, Computers & Fluids 51 (2011) 184 – 188.

[18] A. V. Kolanjiyil, S. Hosseini, A. Alfaifi, D. Farkas, R. Walenga, A. Babiskin, M. Hindle, L. Golshahi, P. W. Longest, Validating cfd predictions of nasal spray deposition: Inclusion of cloud motion effects for two spray pump designs, Aerosol Science and Technology 56 (2022) 305–322.

[19] M. Kiaee, H. Wachtel, M. L. Noga, A. R. Martin, W. H. Finlay, Regional deposition of nasal sprays in adults: A wide ranging computational study, International Journal for Numerical Methods in Biomedical Engineering 34 (2018) e2968.

[20] C. J. Roy, W. L. Oberkampf, A comprehensive framework for verification, validation, and uncertainty quantification in scientific computing, Computer methods in applied mechanics and engineering 200 (2011) 2131–2144.

[21] American Society of Mechanical Engineers, Assessing Credibility of Computational Modeling through Verification and Validation: Application to Medical Devices - V V 40 - 2018, Asme V&V 40-2018 (2018) 60.

[22] American Society of Mechanical Engineers, Standard for Verification and Validation in Computational Fluid Dynamics and Heat Transfer: ASME V&V 20, The American Society of Mechanical Engineers (ASME) (2009).

[23] C. Rigaut, L. Deruyver, J. Goole, B. Haut, P. Lambert, Instillation of a dry powder in nasal casts: parameters influencing the olfactory deposition with uni-and bi-directional devices, Frontiers in Medical Technology 4 (2022).

[24] R. J. A. England, J. J. Homer, L. C. Knight, and S. R. Ell., Nasal ph measurement: a reliable and repeatable parameter, Clinical Otolaryngology Allied Sciences 24 (1999) 67–68.

[25] L. Joris, I. Dab, and P. M. Quinton, Elemental composition of human airway surface fluid in healthy and diseased airways, American Review of Respiratory Disease 148 (1993) 1633–1637. PMID: 8256912.

[26] E. Puchelle, J. M. Zahm, and C. Duvivier, Spinability of bronchial mucus. relationship with viscoelasticity and mucous transport properties., Biorheology 20 (1983) 239–249.

[27] S. Budavari, Merck index 12th ed. whitehouse station, nj: Merck & co, 1996.

[28] H. Calmet, A. M. Gambaruto, A. J. Bates, M. Vazquez, G. Houzeaux, D. J. Doorly, Large-scale cfd simulations of the transitional and turbulent regime for the large human airways during rapid inhalation, Computers in Biology and Medicine 69 (2016) 166–80.

[29] C. E. Rennie, K. A. Gouder, D. J. Taylor, N. S. Tolley, R. C. Schroter, D. J. Doorly., Nasal inspiratory flow: at rest and sniffing., Int Forum Allergy Rhinol 1 (2011) 128–135.

[30] M. Vázquez, G. Houzeaux, S. Koric, A. Artigues, J. Aguado-Sierra, R. Arís, D. Mira, H. Calmet, F. Cucchietti, H. Owen, et al., Alya: Multiphysics engineering simulation toward exascale, Journal of Computational Science 14 (2016) 15–27.

[31] F. Nicoud, F. Ducros, Subgrid-scale stress modelling based on the square of the velocity gradient tensor, Flow, Turbulence and Combustion 62 (1999) 183–200.

[32] P. Koullapis, S. C. Kassinos, J. Muela, C. Perez-segarra, J. Rigola, O. Lehmkuhl, Y. Cui, M. Sommerfeld, J. Elcner, M. Jicha, I. Saveljic, N. Filipovic, F. Lizal, L. Nicolaou, European Journal of Pharmaceutical Sciences Regional aerosol deposition in the human airways : The SimInhale benchmark case and a critical assessment of in silico methods (2017).

[33] O. Lehmkuhl, G. Houzeaux, H. Owen, G. Chrysokentis, I. Rodriguez, A low-dissipation finite element scheme for scale resolving simulations of turbulent flows, Journal of Computational Physics 390 (2019) 51 – 65.

[34] J. Xi, P. W. Longest, Characterization of submicrometer aerosol deposition in extrathoracic airways during nasal exhalation, Aerosol Science and Technology 43 (2009) 808–827.

[35] A. Dastan, O. Abouali, G. Ahmadi, Cfd simulation of total and regional fiber deposition in human nasal cavities, Journal of Aerosol Science 69 (2014) 132 – 149.

[36] J. H. Zhu, H. P. Lee, K. M. Lim, S. J. Lee, D. Y. Wang, Evaluation and comparison of nasal airway flow patterns among three subjects from caucasian, chinese and indian ethnic groups using computational fluid dynamics simulation, Respiratory Physiology & Neurobiology 175 (2011) 62 – 69.

[37] C. O, S. Badia, R. Codina, J. Principe, Assessment of variational multi-

scale models for the large eddy simulation of turbulent incompressible flows, Computer Methods in Applied Mechanics and Engineering 285 (2015) 32–63.

[38] G. Houzeaux, J. Principe, A variational subgrid scale model for transient incompressible flows, IJCFD 22 (2008) 135–152.

[39] G. Ganser, A rational approach to drag prediction of spherical and nonspherical particles, Powder Technology 77 (1993) 143–152.

[40] H. Calmet, C. Kleinstreuer, G. Houzeaux, A. Kolanjiyil, O. Lehmkuhl, E. Olivares, M. Vázquez, Subject-variability effects on micron particle deposition in human nasal cavities, Journal of Aerosol Science 115 (2018) 12–28.

[41] H. Calmet, G. Houzeaux, M. Vázquez, B. Eguzkitza, A. Gambaruto, A. Bates, D. Doorly, Flow features and micro-particle deposition in a human respiratory system during sniffing, Journal of Aerosol Science 123 (2018) 171–184.

[42] M. C. Fung, K. Inthavong, W. Yang, P. Lappas, J. Tu, External characteristics of unsteady spray atomization from a nasal spray device, Journal of Pharmaceutical Sciences 102 (2013) 1024–1035.

[43] B. Adams, W. Bohnhoff, K. Dalbey, M. Ebeida, J. Eddy, M. Eldred, R. Hooper, P. Hough, K. Hu, J. Jakeman, et al., Dakota, A Multilevel Parallel Object-Oriented Framework for Design Optimization, Parameter Estimation, Uncertainty Quantification, and Sensitivity Analysis: Version 6.13 User's Manual., Technical Report, Sandia National Lab.(SNL-NM), Albuquerque, NM (United States), 2020.

[44] A. Santiago, C. Butakoff, B. Eguzkitza, R. A. Gray, K. May-Newman, P. Pathmanathan, V. Vu, M. Vázquez, Design and execution of a verification, validation, and uncertainty quantification plan for a numerical model of left ventricular flow after lvad implantation, bioRxiv (2021).

[45] H. Calmet, K. Inthavong, H. Owen, D. Dosimont, O. Lehmkuhl, G. Houzeaux, M. Vazquez, Computational modelling of nasal respiratory flow, Computer methods in biomechanics and biomedical engineering 24 (2020) 440–458.

[46] Uncertainty quantification types of uncertainty, https://dictionary.helmholtz-uq.de/content/types.html, 2022.

[47] C. J. Freitas, The issue of numerical uncertainty, Applied Mathematical Modelling 26 (2002) 237–248.

[48] J. T. Kelly, B. Asgharian, J. S. Kimbell, B. A. Wong, Particle deposition in human nasal airway replicas manufactured by different methods. part i: Inertial regime particles, Aerosol Science and Technology 38 (2004) 1063–1071.

[49] P. W. Longest, L. T. Holbrook, In silico models of aerosol delivery to the respiratory tract—development and applications, Advanced drug delivery reviews 64 (2012) 296–311.

[50] M. D. Manniello, S. Hosseini, A. Alfaifi, A. R. Esmaeili, A. V. Kolanjiyil, R. Walenga, A. Babiskin, D. Sandell, R. Mohammadi, T. Schuman, et al., In vitro evaluation of regional nasal drug delivery using multiple anatomical nasal replicas of adult human subjects and two nasal sprays, International Journal of Pharmaceutics 593 (2021) 120103.

[51] I. M. Sobol, Sensitivity estimates for nonlinear mathematical models, Mathematical Modelling and Computational Experiments 1 (1993) 407–414.

[52] S. K. Robinson, Coherent motions in the turbulent boundary layer, Annual review of fluid mechanics 23 (1991) 601–639.

[53] U. Piomelli, E. Balaras, Wall-layer models for large-eddy simulations, Annual review of fluid mechanics 34 (2002) 349–374.

[54] K. Inthavong, A. Chetty, Y. Shang, J. Tu, Examining mesh independence

for flow dynamics in the human nasal cavity, Computers in Biology and Medicine 102 (2018) 40–50.

[55] G. Houzeaux, R. Aubry, M. Vázquez, Extension of fractional step techniques for incompressible flows: The preconditioned orthomin(1) for the pressure schur complement, Computers & Fluids 44 (2011) 297–313.

[56] F. Capuano, G. Coppola, L. Rández, L. D. Luca, Explicit Runge – Kutta schemes for incompressible flow with improved energy-conservation properties, Journal of Computational Physics 328 (2017) 86–94.

[57] F. X. Trias, O. Lehmkuhl, A Self-Adaptive Strategy for the Time Integration of Navier-Stokes Equations, Numerical Heat Transfer, Part B: Fundamentals 60 (2011) 116–134.

[58] D. J. Hsu, M. H. Chuang, In-vivo measurements of micrometer-sized particle deposition in the nasal cavities of taiwanese adults, Aerosol Science and Technology 46 (2012) 631–638.

[59] J. D. Schroeter, G. J. M. Garcia, J. S. Kimbell, Effects of surface smoothness on inertial particle deposition in human nasal models, Journal of Aerosol Science 42 (2011) 52–63.

[60] Y. Shang, K. Inthavong, J. Tu, Detailed micro-particle deposition patterns in the human nasal cavity influenced by the breathing zone, Computers & Fluids 114 (2015) 141 – 150.

[61] H. Shi, C. Kleinstreuer, Z. Zhang, Modeling of inertial particle transport and deposition in human nasal cavities with wall roughness, Journal of Aerosol Science 38 (2007) 398–419.

[62] H. Bahmanzadeh, O. Abouali, M. Faramarzi, G. Ahmadi, Numerical simulation of airflow and micro-particle deposition in human nasal airway pre- and post-virtual sphenoidotomy surgery, Computers in Biology and Medicine 61

(2015) 8 – 18.

[63] E. Ghahramani, O. Abouali, H. Emdad, G. Ahmadi, Numerical investigation of turbulent airflow and microparticle deposition in a realistic model of human upper airway using les, Computers & Fluids 157 (2017) 43–54.

[64] T. Homma, A. Saltelli, Importance measures in global sensitivity analysis of nonlinear models, Reliability Engineering System Safety 52 (1996) 1–17.

Appendix

Mesh parameters

An unstructured mesh with prism layers is created using ANSYS-ICEM-CFD (Ansys Inc., USA). The octree-based method generated a fine resolution surface mesh with surface smoothing to maintain smooth transitions between mesh sizes. The volume is filled with tetrahedral cells with a smooth cell transition ratio of 1.2 employed close to the boundary wall, using the Delaunay method. The final step inserted prism layers at the near wall boundaries to resolve high velocity gradients at the wall. The mesh parameter used in this study is given in Table 9.

Mesh	$N_N(\times 10^6)$	$N_E(\times 10^6)$	$\Delta(mm)$	N_{pl}	$h_{pl}(mm)$
M1	1.3	4.2	0.7	5	0.5

Table 9: Summary of different mesh resolutions with N_N: number of nodes, N_E: number of elements, Δ: average grid size, N_{pl}: number of prism layers and h_{pl}: height of total prism layer.

A minimum element height of 26µm at the wall is applied on the nasal valve, which is the most critical region due to the constriction. This produced a range of $y^+ = \frac{u_* y}{\nu}$ =1 to 3 which was the maximum velocity during sniffing, Q_{max} = 60L/min. The term u_* is the friction velocity at the wall, y is the distance to the wall and ν is the local kinematic viscosity of the fluid. The values of y^+ are considered sufficiently small for resolving the near-wall flow dynamics ([52]) and falls into the range defined by [53] that describes well resolved wall-layers.

The mesh convergence is based on the mesh element size evaluated with similar flow rate producing the same range of Reynolds number on the nasal cavity in earlier studies by the authors [28, 12] or other works as [54]. We used a minimum scoped mesh element size of 0.5 mm in the nasal cavity region to insure the grid is sufficiently fine for LES method.

Governing equations

In this section, we describe the numerical method used to solve the Navier-Stokes equations. The software employed is the high performance computational mechanics code Alya ([30]), which was developed at Barcelona Supercomputing Center. Let μ be the dynamic viscosity of the fluid, and ρ its constant mass density. The problem is stated as follows: find the velocity $\boldsymbol{u}$ and mechanical pressure p in a domain Ω such that they satisfy in a time interval $[t_0, t]$,

$$\rho \frac{\partial \boldsymbol{u}}{\partial t} + \rho(\boldsymbol{u} \cdot \nabla)\boldsymbol{u} - \nabla \cdot [2\mu \boldsymbol{\varepsilon}(\boldsymbol{u})] + \nabla p = \boldsymbol{0}, \tag{4}$$

$$\nabla \cdot \boldsymbol{u} = 0, \tag{5}$$

together with initial and boundary conditions,

$$\boldsymbol{u}(t_0) = \boldsymbol{u}_0, \tag{6}$$

$$\boldsymbol{u} = \boldsymbol{u}_D \qquad \forall \boldsymbol{x} \in \partial\Omega_D, \tag{7}$$

$$\boldsymbol{\sigma} \cdot \boldsymbol{n} = 0 \qquad \forall \boldsymbol{x} \in \partial\Omega_N, \tag{8}$$

where the velocity strain rate is $\boldsymbol{\varepsilon}(\boldsymbol{u}) = \frac{1}{2}(\nabla \boldsymbol{u} + \nabla \boldsymbol{u}^t)$, $\boldsymbol{u}_0$ gives the initial velocity, $\boldsymbol{u}_D$ the Dirichlet boundary conditions imposed on $\partial\Omega_D$, while $\partial\Omega_D$ are the Neumann boundaries with external normal $\boldsymbol{n}$, and $\boldsymbol{\sigma} = -p\boldsymbol{I} + \boldsymbol{\varepsilon}(\boldsymbol{u})$ is the Cauchy stress tensor.

Implicit LES

The numerical model of the Navier-Stokes solver is a stabilized finite element method, based on the Variational MultiScale (VMS) method ([38]) which is considered an implicit Large Eddy Simulation.

The discretization of the Navier-Stokes equations yields a coupled algebraic sys-

tem to be solved at each linearization step within a time loop. The resulting system is split to solve the momentum and continuity equations independently. This is achieved by applying an iterative strategy to solve for the Schur complement of the pressure. According to our scheme, at each linearization step it is necessary to solve the momentum and continuity equation twice. This split strategy is described and validated in [55].

LES

The spatially filtered Navier-Stokes equations for a fluid moving in the domain Ω bounded by $\Gamma = \partial\Omega$ during the period (t_0, t_f) repose to find a filtered velocity $\overline{\mathbf{u}}$ and a kinematic pressure p such that

$$\partial_t \overline{\mathbf{u}} + (\overline{\mathbf{u}} \cdot \nabla)\overline{\mathbf{u}} - 2\nu\nabla \cdot \mathbf{S}(\overline{\mathbf{u}}) + \nabla p - \mathbf{f} = -\nabla \cdot \tau_{\mathbf{ij}}(\overline{\mathbf{u}}) \qquad \text{in } \Omega \times (t_0, t_f), \tag{9}$$

$$\nabla \cdot \overline{\mathbf{u}} = 0 \qquad \text{in } \Omega \times (t_0, t_f), \tag{10}$$

where ν is the fluid viscosity, $\mathbf{f}$ the vector of external body forces and $\mathbf{S}(\overline{\mathbf{u}})$ is the large-scale rate-of-strain tensor. In equation (9) $\tau_{\mathbf{ij}}(\overline{\mathbf{u}})$ is the subgrid scale (SGS) stress tensor, which must be modelled. Its deviatoric part is given by

$$\tau_{\mathbf{ij}}(\overline{\mathbf{u}}) - \tfrac{1}{3}\tau_{\mathbf{kk}}(\overline{\mathbf{u}})\delta_{\mathbf{ij}} = -2\nu_{sgs}\nabla \cdot \mathbf{S}(\overline{\mathbf{u}}) \tag{11}$$

where $\delta_{\mathbf{ij}}$ is the Kronecker delta. The formulation is closed by an appropriate expression for the subgrid-scale viscosity, ν_{sgs}. In this study the wall-adapting local-eddy viscosity model (WALE)[31] is applied. This model provided good results in previous simulations of respiratory airways being competitive comparing with more computational demanding models like the dynamic Smagorinsky, see [32].

The set of equations is time integrated using an energy conserving Runge-Kutta explicit method, lately proposed by Capuano et al.[56], combined with an eigenvalue-based time step estimator[57]. For more details about LES method see [33].

Validation of micro-particle deposition

Micro particle deposition in the nasal cavity was compared to experimental data reported by [48, 58] and numerical data [59, 60, 61] (see Fig 9) where the flow rate used for the comparison was a constant 20L/min. In order to standardize the results, the inertial parameter (IP) was used, *i.e*:

$$IP = d_p^2 \cdot Q \tag{12}$$

where d_a is the particle aerodynamic diameter (*i.e*: $1\,\mathrm{g\,cm^{-3}}$) and Q is the volumetric flow rate. Fig 9 shows good agreement between the simulation performed by the present code (Alya) and the numerical results of [59, 60, 61]. Differences in deposition results are due to the coarser airway surfaces in the replica producing higher deposition efficiencies than the numerical model, already observed frequently in literature, see [61, 62] who provide an extended study which can be summarized as the "wall roughness region enhanced particle capturing effect" or other study [63] who compared deposition of different level of surface roughness replicas (see Fig 9 Model A,B,C) from [48] with LES simulations.

Sobol indices

As mentioned above, the Sobol indices quantify the effect of uncertainty in knowledge of inputs on the variance of the outputs of a model [51]. Given a model f for

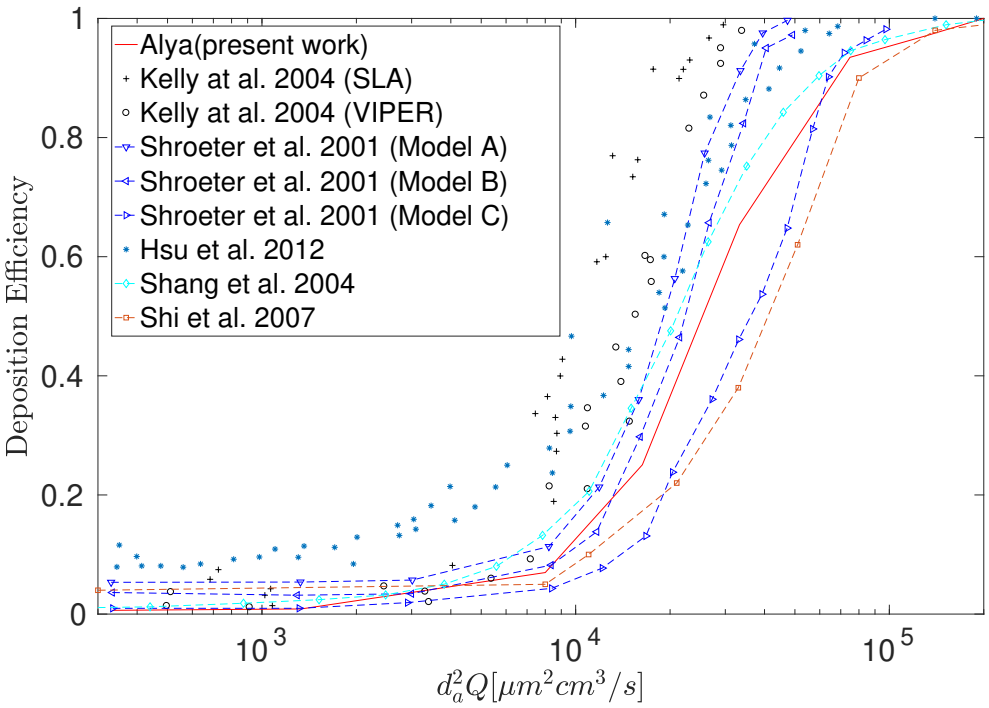

Figure 9: Micro particle deposition efficiency comparison between simulation and experiments.

the output scalar variable Y,

$$Y = f(X_1, ..., X_p), \tag{13}$$

the input variables $X_1, ..., X_p$ can be described by probability distributions which reflect the uncertainty in knowledge of the system. The importance of each input variable X_i on the variance of Y can be quantified by evaluating the expected value of the conditional variance of Y given X_i,

$$E_{X_i}(V_{\boldsymbol{X}_{-i}}(Y|X_i)), \tag{14}$$

where the variance is taken over the $(p-1)$-dimensional parameter space $\boldsymbol{X}_{-i}$ which includes all inputs except for X_i. Using the law of total variance and normalizing, the first-order Sobol index writes

$$S_i(Y) = \frac{V_{X_i}(E_{\boldsymbol{X}_{-i}}(Y|X_i))}{V(Y)}. \tag{15}$$

This index is useful, but does not account for the effects of the interactions between X_i and $X_j \in \boldsymbol{X}_{-i}$ on Y. Homma and Saltelli [64] introduced the total Sobol index, which does account for all the contributions of X_i and its interactions, to the output Y, and is defined as:

$$ST_i(Y) = \frac{E_{\boldsymbol{X}_{-i}}(V_{X_i}(Y|\boldsymbol{X}_{-i}))}{V(Y)} \tag{16}$$

These are the indices shown in Figure 8 in the study.